

Unlocking the Potential: Multi-task Deep Learning for Spaceborne Quantitative Monitoring of Fugitive Methane Plumes

Guoxin Si, Shiliang Fu, and Wei Yao *Senior Member, IEEE*

Abstract—With the intensification of global warming, the monitoring of methane emission and detection of gas plumes from landfills have increasingly received attention. We decompose the methane emission monitoring into three sub-tasks: methane concentration inversion, methane plume segmentation, and methane plume emission rate estimation. Conventional algorithms for these tasks have limitations: methane concentration inversion commonly uses the matched filter algorithm (e.g. MAG1C), which is sensitive to the global spectrum distribution and contains a large amount of noises in inversion results. There is limited research on methane plume segmentation, with many studies resorting to manual segmentation that are most likely subjective. The estimation of methane point-source emission rate often utilizes the IME algorithm, which relies on obtaining accurate meteorological measurement data, such as wind speed, and thus is not widely applicable. Using the WENT landfill site in Hong Kong as test site and PRISMA hyperspectral satellite imagery as data source, we propose a new deep learning-based framework for quantitative monitoring of methane emissions from hyperspectral remote sensing images based on physical simulation. We generate simulated methane plumes using large eddy simulation (LES) and different concentration maps of fugitive methane emission using the radiative transfer equation (RTE), while combining augmentation techniques to create a simulated PRISMA dataset. We train a U-Net network for methane concentration inversion, a Mask R-CNN network for methane plume segmentation, and a ResNet-50 network for methane emission rate estimation. All of these three deep networks achieve higher validation accuracy compared to conventional algorithms. We further respectively combine the first two sub-tasks and the last two sub-tasks to design the multi-task learning models - MTL-01 and MTL-02, both of which achieve higher accuracy than single-task models. Our research serves as a demonstration of applying multi-task deep learning to quantitative methane monitoring and can be extended to a broad range of methane monitoring tasks.

Index Terms—Methane plume, Hyperspectral remote sensing, Simulation, Multi-task deep learning.

I. INTRODUCTION

Currently, landfills are still widely used around the world [28][52]. It is estimated that about 40-50% of the greenhouse gases emitted by landfills are methane [2]. Landfills account for approximately 5% of global methane emissions and are considered one of the largest anthropogenic sources of CH_4 [39]. Furthermore, their contribution to atmospheric methane has been increasing since the beginning of the 21st century [4]. The emission of greenhouse gases, including

methane, not only affects the surrounding ecological environment [20] but also has the potential to exacerbate extreme weather events in urban areas [50]. From 1960 to 2019, the radiation stress contribution of methane accounted for 11% of the total radiation stress, making it the second largest greenhouse gas after carbon dioxide. Compared to other main greenhouse gases, such as carbon dioxide and nitrous oxide, methane has a relatively short atmospheric lifetime of approximately 9.14 years [4]. This implies that reducing methane emissions may have a quicker impact on alleviating global warming compared to reducing emissions of other greenhouse gases.

To detect emitted methane plumes, airborne data (AVIRIS-NG) is commonly utilized due to small-scale methane emission sources [9][10]. However, the advent of PRISMA, a new generation hyperspectral satellite with a 30m spatial resolution, has now made it feasible for spaceborne methane emission retrieval [6]. The process of methane plume monitoring can be divided into three tasks: (1) methane concentration inversion, (2) methane plume segmentation, and (3) flux rate estimation of single plumes. For methane concentration inversion, current methods predominantly rely on differential optical absorption spectroscopy (DOAS) and matched filter techniques. DOAS, although computationally intensive, is typically employed for small-scale inversion in scenarios where emission point-sources are known [44][45]. On the other hand, matched filter algorithms are commonly applied for large-scale methane plume screening [10][43]. However, it is important to note that the accuracy of the matched filter algorithm heavily relies on precise target spectrum modeling and background estimation [10][42].

There have been few studies conducted on methane plume segmentation, but it is crucial to accurately delineate single plumes as it significantly determine the accuracy of methane flux rate estimation. Over the past few decades, a plethora of algorithms for estimating point source emission rates have been proposed. However, most of these algorithms require local wind speed data as auxiliary information, which is challenging to obtain due to the limited availability of meteorological observation stations[47]. [23] addressed this limitation by employing simulated plumes and deep learning techniques to estimate emission rates without the need for wind speed information, although the presented network could only estimate the emission rate of single-source plumes. In practical scenarios, it is often necessary to segment individual plumes from an image and estimate the emission rates separately.

G.Si, S.Fu and W.Yao are with Department of Land Surveying and Geo-Informatics, The Hong Kong Polytechnic University, Hong Kong e-mail: (wei.hn.yao@polyu.edu.hk).

Manuscript received April 19, 2005; revised September 17, 2014.

Since the introduction of AlexNet in 2012, deep learning has witnessed rapid development and yielded remarkable results in various remote sensing application fields[24][21][22]. The U-net deep learning architecture was initially designed for semantic segmentation tasks[35][31], but it also exhibits enormous potential for regression[38]. We regard methane concentration inversion as pixel-by-pixel regression, so U-net can be used to complete the task. Additionally, Mask R-CNN has proven to be highly effective in a wide range of instance segmentation tasks and should also be applicable to Methane plume segmentation. Moreover, ResNet addresses the issue of gradient vanishing, enabling deeper networks to improve feature extraction capabilities[16][37]. Many of former works for emission rate estimation using shallow convolutional neural networks(CNN) has proven successfully realizable but with moderate accuracy[15]. It is reasonable to apply ResNet to enhanced emission rate estimation. And our goal is to leverage physically simulated plumes as training data for multi-task deep learning techniques to simultaneously perform methane concentration inversion, methane plume segmentation, and flux rate estimation in a unified approach.

The major contributions of this paper are as follows:

1. We propose a physics-informed deep learning scheme for spaceborne retrieval of methane emissions based on data simulation using Large Eddy Simulation (LES), Radiative Transfer Equation (RTE), and data augmentation techniques.
2. We apply instance segmentation algorithm to solve the problem of isolating and identifying methane emission sources by plume segmentation.
3. We show that the serialization of multiple sub-tasks for methane emission monitoring will lead to additional error accumulation, and designed multi-task learning model to suppress the errors.

II. METHOD

In this section, we present the principles of simulation, methane concentration inversion, methane plume segmentation, and methane concentration estimation. The two multi-task deep learning networks and relevant training mechanisms that we have designed are also presented.

A. Simulation

The simulation operation consists of two parts: simulation of methane plume emission and simulation of PRISMA-like satellite images with methane plume signal. For methane plume simulation, we utilized Large Eddy Simulation (LES), which is a computational fluid dynamics (CFD) method used to simulate turbulent phenomena in fluid flow[36]. It combines the advantages of Direct Numerical Simulation (DNS) and Reynolds-Averaged Navier-Stokes equations (RANS) methods, aiming to accurately predict the statistical characteristics of turbulent flow[32][8]. The core of LES lies in filtering the flow field into large and small-scale vortices through a filtering operation. This can be achieved by applying a low-pass filter to remove high-frequency small-scale vortices, while retaining the low-frequency large-scale vortices[8]. The filtered flow field equations form the basis of LES. The governing equations

for LES are based on the Reynolds-averaged Navier-Stokes equations (RANS)[12], which are solved to simulate the motion and turbulent effects in the fluid [1]:

$$\frac{\partial \bar{u}_i}{\partial t} + \frac{\partial}{\partial x_j}(\bar{u}_i \bar{u}_j) = -\frac{1}{\rho} \frac{\partial \bar{p}}{\partial x_i} + \nu \frac{\partial^2 \bar{u}_i}{\partial x_j \partial x_j} - \frac{\partial}{\partial x_j}(\bar{u}_i' u_j') \quad (1)$$

where \bar{u}_i is the time-average speed, t is the temporal change in fluid motion, x_i is the position of the fluid in a certain direction, \bar{p} is the average pressure of a fluid at a location, ρ is fluid density, ν is kinematic viscosity, and $\bar{u}_i' u_j'$ is the reynolds stress.

For simulation of PRISMA remote sensing images with methane plumes, we merged synthetic plume signals with real PRISMA remote sensing data[4]. First, plumes of different shapes, sizes, and concentrations through simulation were generated and assigned corresponding spectral characteristics based on physical radiation properties. Then, we fused the synthetic plumes with real PRISMA remote sensing images to generate simulated images with realistic background textures and synthetic methane spectrum. Such simulated images are crucial for training and evaluating our algorithms as they can simulate real observation scenarios under controlled experimental conditions[9]:

$$r' = (1 - s)r \quad (2)$$

where r denotes the PRISMA image background spectrum without noise and methane signal, r' is the simulated spectrum, s is the simulated methane absorption cross-section. And s is generated by summation of the radiative transfer equation (RTE), multiplied by the layered methane concentration and corresponding dry air density.

By combining these two steps, we are able to simulate methane plumes of various shapes, sizes, and concentrations and inject them into PRISMA data to generate simulated hyperspectral satellite images, which contain methane plume signal overlaid with realistic scene background. This provides a solid foundation for our research and allows us to validate the performance and reliability of our methodology in real-world scenarios.

B. Methane Concentration Inversion

Maglc is a matched filter method that effectively aligns trace gas concentration path lengths by incorporating sparsity and reflectivity correction. Maglc is also one of the most advanced matched filter methods currently and provides a mature and operational software interface[10]. The calculation formula for Maglc is as follows[9]:

$$a = \frac{(L_i - u)^T C^{-1}(t(u))}{(t(u))^T C^{-1}(t(u))} \quad (3)$$

where a is methane concentration, L is radiation intensity, $t(u)$ is mean radiation, and C is covariance matrix.

Considering the intricate distribution of land and sea areas in Hong Kong, as well as the challenging rugged terrain and dense urban construction, it can be expected that the surface conditions in the region significantly influence the outcomes of

methane concentration inversion. To address this, we propose the utilization of a K-means based masking method to run MagIc and conduct a comparative analysis with alternative algorithms[11].

The U-net is a deep learning network characterized by encoding-decoding structure and is primarily used for semantic segmentation tasks[35][31][51]. Typically, the input and output channels of the U-net are of equal size. However, to accommodate the requirements of methane concentration inversion, an additional layer of $1 * 1$ convolution is added after the U-net encoding-decoding structure[25], and the loss function for the regression task is replaced. The employed loss functions include Mean Squared Error (MSE) and $SmoothL_1$:

$$loss_{mse} = \frac{1}{n} \sum_{i=1}^n (y_i - \hat{y}_i)^2 \quad (4)$$

$$loss_{SmoothL_1} = \begin{cases} \frac{1}{2}(y - \hat{y})^2 & \text{if } |y - \hat{y}| < 1 \\ |y - \hat{y}| - \frac{1}{2} & \text{otherwise} \end{cases} \quad (5)$$

where y is the true label, \hat{y} is the predicted value, n is the number of samples, and $|y - \hat{y}|$ represents the absolute difference between y and \hat{y} .

Before initiating the training process, the images and labels in the training sample dataset are normalized by calculating the mean and standard deviation of all bands. The network is trained using two loss functions, MSE and SmoothL1, with an initial learning rate of 0.001. The learning rate reduces by 90

C. Methane Plume Segmentation

Instance segmentation is a classical task in computer vision, and methane plume segmentation is essentially an instance segmentation task. Previous research works on methane plume segmentation are limited, and many studies rely on subjective segmentation criterion[14]. Some of studies suggested using traditional algorithms for methane plume segmentation, with contour tracing algorithms being considered as a good choice due to its efficiency and stability. On the other hand, there are many deep learning-based instance segmentation algorithms, among which Mask R-CNN is the most classical and widespread one[17]. It is a two-step instance segmentation algorithm that has proven to achieve high performance on a large amount of datasets for a wide range of applications. Although new instance segmentation algorithms are continuing to emerge, some of the algorithms sacrifice segmentation accuracy for real-time segmentation[40], which is not necessarily required for our case. Other algorithms may achieve higher instance segmentation accuracy[49], but require increasingly complex optimization processes during training, which is not cost-effective for our case. Therefore, we chose Mask R-CNN as the deep learning algorithm for methane plume segmentation, and active contour algorithms as the traditional counterpart algorithm. Typically, Mask R-CNN takes three image channels as inputs, but we modified the input layer to allow for flexible alteration between one or 49 input channels so as to accommodate different segmentation requirements. We used the original loss function of Mask R-CNN:

$$L = L_{cls} + L_{box} + L_{mask} \quad (6)$$

where L is the total loss function, L_{cls} is the category loss function, which is based on the cross entropy loss, L_{box} is the bounding box loss function, which is based on the $SmoothL_1$ loss, and L_{mask} is the mask loss function, which typically uses the binary cross entropy:

$$L_{cls} = - \sum_{i=1}^N y_i \log(\hat{y}_i) \quad (7)$$

where y_i denotes the true label, \hat{y}_i is the probability predicted by the model, and N is the number of samples.

$$L_{box} = \sum_{i=1}^N smooth_{L_1}(x_i - \hat{x}_i) \quad (8)$$

$$L_{box} = -IoU(b, \hat{b}) + \frac{\rho^2(b, \hat{b})}{c^2} \quad (9)$$

where b and \hat{b} respectively denotes the ground truth bounding box and the predicted bounding box, $IoU(b, \hat{b})$ indicates the intersection over union between these two bounding boxes, $\rho^2(b, \hat{b})$ is the Euclidean distance between the center points of two bounding boxes, and c is a hyperparameter typically set to 10.

D. Methane Emission Rate Estimation

There are two scenarios for estimating emission rates. The first scenario involves estimating emission rates using training samples specifically gathered for this purpose. The goal here is to assess the performance of estimation algorithm under ideal conditions. The second scenario refers to estimating emission rates based on plume segmentation results, where the objective is to evaluate and enhance the accuracy of plume instance segmentation algorithms.

The emission rate of a methane plume is commonly estimated using the integrated mass enhancement (IME) mode[15]. This mode involves following calculations:

$$Q = \frac{U_{eff} \cdot IME}{L} \quad (10)$$

where U_{eff} is the effective wind speed, L is the plume length, IME refers to the integrated mass enhancement. And the calculations for U_{eff} , L , and IME are as follows[47][15]:

$$U_{eff} = 0.34 \cdot U_{10} + 0.44 \quad (11)$$

where U_{10} is the wind speed at 10 meters.

$$L = \sqrt{A_M} \quad (12)$$

where $\sqrt{A_M}$ is the area of a plume.

$$IME = k \sum_{i=1}^{n_p} \hat{\alpha}(i) \quad (13)$$

where n_p is the number of pixels in a plume, $\hat{\alpha}(i)$ is the value of i th pixel, and k is a scale factor equal to $5.155 \cdot 10^{-3} kg/ppb$.

ResNet is a deep learning method by utilizing residual blocks, which enables the neural network to learn the residual map by effectively avoiding issues such as gradient vanishing

and explosion[16]. ResNet is widely applied in various application fields, including image recognition, object detection, and speech processing, yielding impressive results[48][37]. We conducted training on emission rate estimation samples for ResNet-50 network to perform the flux rate estimation task. Subsequently, ResNet-50 was used as a pretrained network to validate the reasonability of plume segmentation results and assist in optimizing the instance segmentation network.

E. Multi-task Learning I (MTL-01)

Through experiments, it was found that during the serial prediction process using Mask R-CNN followed by ResNet-50, false positives and false negatives of Mask R-CNN would introduce significant errors to the emission rate estimation (Fig. 9), although such errors may be acceptable for plume segmentation task. To address this issue, we propose a multi-task network called MTL-01, which simultaneously trains Mask R-CNN and ResNet-50 to learn.

Considering that the loss function of Mask R-CNN measures instance segmentation and does not consider error propagation, we design a serial network (MTL-01), which takes the segmentation results of Mask R-CNN as input to ResNet-50 and calculates additional loss terms for back-propagation to assist in optimizing the Mask R-CNN (Fig. 1). The ResNet-50 in the serial network is a pre-trained model, whose parameters are not updated. During the training process, the erroneous (over-)segmentation masks from Mask R-CNN are mainly categorized into two types. The first type is small false positive patches escaping from NMS(Non-Maximum Suppression) filtering[17], which were only found to slightly contribute to errors in subsequent emission rate estimation rather than main error source of the serial network. From simulation experiments, it is observed that the size of plumes are rarely smaller than 300 pixels, so we ignore the false positive patches smaller than 300 pixels and resolve this kind of error with an object detection loss term. The second type is large false positive patches, which are often wrongly separated from overlapping plumes and lead to significant errors in emission rate estimation. To address the issue, we design an additional loss term, $loss_{ER}$, for MTL-01. $loss_{ER}$ still uses smoothL1 as the basis, but the segmentation results less than 300 pixels do not participate in the calculation of $loss_{ER}$, and the missed masks are regarded as an emission rate estimate of 0 kg/h and the loss is calculated accordingly:

$$loss_{ER} = \begin{cases} loss_{SmoothL1}(y_i, \hat{y}_i) & \text{if } y_i \in TP \\ loss_{SmoothL1}(0, \hat{y}_i) & \text{if } y_i \in FP \end{cases} \quad (14)$$

In MTL-01, we consider the $loss_{ER}$ term as a corrected loss term and assign it a coefficient lambda, while the original loss function of Mask R-CNN remains unchanged. Therefore, the loss function of MTL-01 is as follows:

$$loss_{MTL-01} = loss_{MaskR-CNN} + \lambda \cdot loss_{ER} \quad (15)$$

In this equation, $loss_{MaskR-CNN}$ denotes the loss function of Mask R-CNN, $loss_{ER}$ denotes the loss function of emission rate estimation, and λ is the coefficient. Based on our experiments, we found that $\lambda = 0.1$ is optimal.

F. Multi-task Learning II (MTL-02)

The methane concentration inversion task predicts pixel-wise values from hyperspectral images, while the methane plume segmentation task also extract plume masks directly from hyperspectral images. They are similar in form and logically related, and it could be possible to obtain higher accuracy by training multi-task learning models for methane concentration inversion and plume segmentation tasks. To this end, we designed a multi-task learning network that incorporates U-net and Mask R-CNN.

In MTL-02(Fig. 2), the network architecture of Mask R-CNN remains unchanged, and the decoding structure of U-net is connected to the backbone network of Mask R-CNN. Considering the output sizes of the stages in the ResNet-50 backbone network, we added an additional output to stage 0 of ResNet-50 to ensure that the size of the U-net decoding result matches the input size, similar to LinkNet[53]. It is worth noting that the deepest output of ResNet-50 is not involved in the construction of the U-net decoding structure but only participates in the FCN[27] structure of Mask R-CNN. Additionally, considering that there is a max-pooling layer between the two outputs of ResNet-50, which may lead to underfitting of the U-net decoding structure, we added an ASPP (Atrous Spatial Pyramid Pooling) layer composed of three dilated convolutions immediately after the U-net decoder, with dilation rates of 1, 2, and 4.

ASPP (Atrous Spatial Pyramid Pooling)[5] is based on dilated convolutions and SPP (Spatial Pyramid Pooling)[18]. It is used to address the contradiction between reducing the feature map resolution as far as possible and capturing a large receptive field when extracting image features. ASPP uses dilated convolutions with different sampling rates to capture the context of a image at multiple scales. In ASPP, different dilated convolutions with different rates are applied to the input feature map and then merged. To enhance the model's receptive field, the output feature maps of the dilated convolution with different sampling rates are average-pooled.

For the loss function of MTL-02, we adopted the classical weighted average of individual loss functions for multiple tasks[46][3]:

$$loss_{MTL-02} = w_1 \cdot loss_{U-net} + w_2 \cdot loss_{MaskR-CNN} \quad (16)$$

where $loss_{U-net}$ is the loss function of U-net, $loss_{MaskR-CNN}$ is the loss function of Mask R-CNN, and w_1 and w_2 are the weights for respective loss component.

To determine the weights of the MTL-02 loss function, we used the Dynamic Weighted Average (DWA) algorithm[26], the idea of which is that different tasks have different levels of difficulty and learning speed. Instead of setting different learning rates for each task, it is better to dynamically adjust the weights to let each task learn at a similar pace. In simple terms, tasks with faster loss reduction are assigned smaller weights, while tasks with slower loss reduction are assigned larger weights.

$$w_k(t) = \frac{K \cdot e^{\frac{\lambda_k(t-1)}{T}}}{\sum_{i=1}^K e^{\frac{\lambda_i(t-1)}{T}}} \quad (17)$$

$$\lambda_k(t-1) = \frac{L_k(t-1)}{L_k(t-2)} \quad (18)$$

where K is the number of tasks, $\lambda_k(t-1)$ denotes the rate of loss reduction for the k -th task during the $(t-1)$ -th training iteration, and $L_k(t-2)$ represents the loss for the k -th task during the $(t-2)$ -th training iteration. When T is a constant, $T=1$ indicates that w is equal to the result of softmax; However, as T increases significantly, w approaches 1, leading to equal loss weights for all tasks.

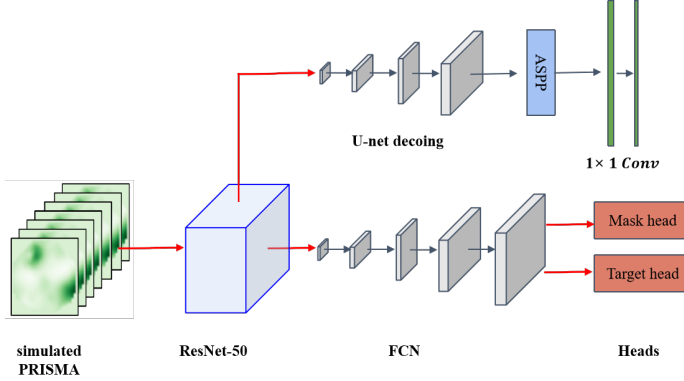


Fig. 2: Multi-task learning II (MTL-02)

III. EXPERIMENTS

A. Research Areas and Data

1) *Research Areas*: Hong Kong, located in the southern region of China, is mostly characterized by hilly terrains. With a high level of urbanization, the climate is humid and rainy, with an average annual precipitation of over 2000 millimeters. In Hong Kong, there are two major landfills, namely Western New Territories (WENT) Landfill and North East New Territories (NENT) landfill. As most of PRISMA images collected are from the WENT region, our research primarily focuses on this area. The Tuen Mun landfill (Fig. 3), covering an approximate area of 27 hectares, is situated in the southwest of Tuen Mun district in close proximity to Shenzhen Bay. It is one of few government-approved waste disposal sites in the Hong Kong Special Administrative Region, primarily receiving municipal solid waste from various regions, including Hong Kong Island, Kowloon, and New Territories.

2) *Data*: The PRISMA satellite was launched on March 22nd, 2019 and offers hyperspectral images of global coverage with a spatial resolution of 30 m. The spectral smile is less than 5 nm, the spectral resolution is better than 12 nm in a spectral range of 400-2500 nm (VNIR and SWIR regions) [6], and datasets are open-access.

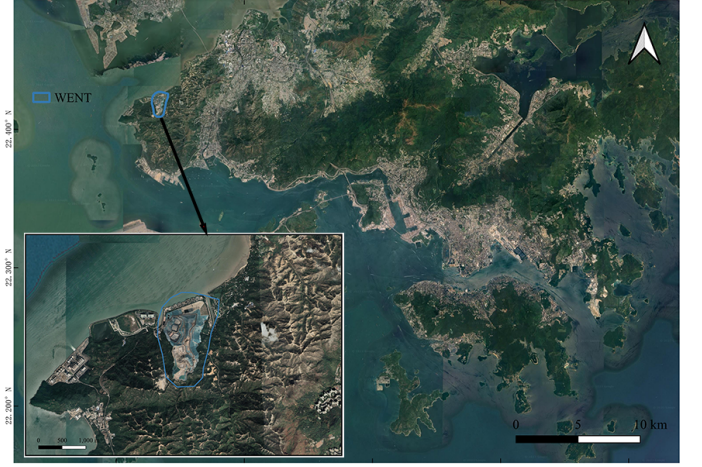


Fig. 3: Research area

We have collected 10 PRISMA images of WENT, which are: 20220102, 20220119, 20220723, 20220914, 20230217, 20230301, 20230307, 20230416, 20230712, 20230724. These raw images will be used for experimental data generation and analysis.

B. Data Curation

We conducted LES simulation of methane plumps at different emission rates and wind speeds using the PALM software[33][30]. Four emission rate gradients were set, namely 500kg/h, 1000kg/h, 1500kg/h, and 2000kg/h. We also considered ten wind speed gradients: 1m/s, 2m/s, 3m/s, 4m/s, 5m/s, 6m/s, 7m/s, 8m/s, 9m/s, and 10m/s. In total, 40 sets of methane plume emission scenarios were simulated (Fig. 4). Among them, the simulated plume emission data with wind speeds of 1m/s, 5m/s, and 10m/s were used to create the validation dataset, while remaining plume emission data were used to create the training dataset. Both training and validation datasets consist of five parts: simulated PRISMA data, corresponding methane concentration distribution data (*Multiplume*), methane concentration distribution data with added random noise (*noisy Multiplume*), segmentation mask

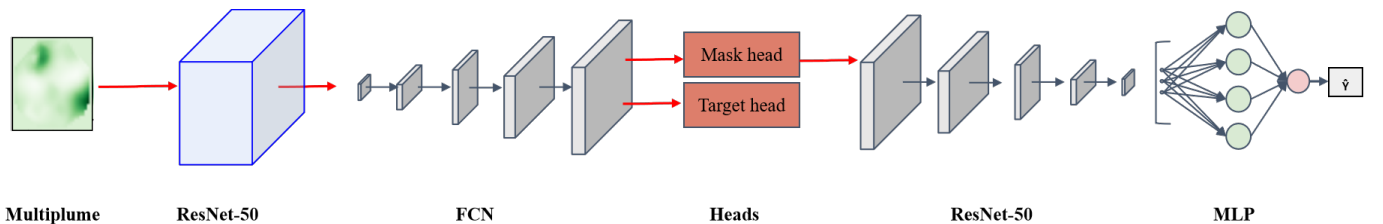


Fig. 1: Multi-task learning I (MTL-01)

boundaries (*Mask label*), and corresponding single plume. Each *Multiplume* and *noisy Multiplume* data corresponded to specific emissions rates (*ER*), while *Mask label*, single plume, and *ER* were also one-to-one correlated. Simulated PRISMA data and *Multiplume* constitute the sample set for methane concentration inversion task, *noisy Multiplume* and *Mask label* constitute the sample set for methane plume segmentation task, single plume and *ER* constitute the sample set for methane plume emission rate estimation task, and *noisy Multiplume*, *Mask label*, and *ER* constitute the sample set for multi-task learning models.

Fig. 5 illustrates the process of creating both training and validation datasets. Initially, ten PRISMA hyperspectral images were selected as base maps, specifically 20220102, 20220119, 20220723, 20220914, 20230217, 20230301, 20230307, 20230416, 20230712, and 20230724. Among them, 20220119, 20220723, and 20230307 were used as base maps for the validation set, while the others were used for the training set. The methane signals detected by using *mag1c* inversion[9] were removed from the PRISMA images [7][45]. Additionally, K-means clustering was applied to classify the images into ocean and land areas (Classified data). The base maps were then segmented into 256*256*band patches with a stride of 50 pixels, and the corresponding Classified data were generated. If the proportion of land in a segmented Classified data patch was less than 70%, the corresponding base map patch would be discarded. Next, we created multi-plume distribution maps (*Multiplume*) by generating a random number between 0 and 3 to determine the number of plumes (*n*). If $n = 0$, the multi-plume distribution map would be all set zeros. If $n > 0$, n enhanced plumes were added to the distribution map[23][13].

The plume enhancement process involved multiplying all pixel values of a plume by a factor b , which also increased the emission rate of the plume by b times. The plume was then subject to random rotations, and a random part of the low-value plume was discarded after rotation. Furthermore, the overlap ratio of two plumes' could not exceed 15%:

$$Overlapratio(A, B) = \frac{\sum_{x_i \in A \cap B} x_i}{\sum_{x_i \in A \cup B} x_i} \quad (19)$$

where A, B represent two 2D plumes, x_i is the pixel value in the plume.

If the conditions were met, the corresponding plume mask file and enhanced plume concentration maps are stored separately. Finally, the methane signals corresponding to the multi-plume distribution map were added to the hyperspectral base map. If the multi-plume distribution map was empty, no action was taken, and the original noise was added to the simulated PRISMA data.

C. Accuracy Assessment

1) *Regression Task*: Both the inversion of methane concentration and estimation of emission rate are integral to the regression mission. Hence, to evaluate the accuracy, we employed the RMSE and MAE metrics.

$$RMSE = \sqrt{\frac{1}{n} \sum_{i=1}^n (y_i - \hat{y}_i)^2} \quad (20)$$

$$MAE = \frac{1}{n} \sum_{i=1}^n |y_i - \hat{y}_i| \quad (21)$$

where y is the ground truth value, \hat{y} is the predicted value, and n is the number of samples.

2) *Segmentation Task*: We use the Average Precision (AP) to measure the accuracy of the methane plume segmentation task. The formula for calculating AP is as follows[19][41]:

1. Set a threshold and determine the number of *TP*, *FP*, *TN*, and *FN* based on the threshold.

TP: True positive, the number of positive samples correctly classified as positive.

FP: False positive, the number of negative samples falsely classified as positive.

TN: True negative, the number of negative samples correctly classified as negative.

FN: False negative, the number of positive samples falsely classified as negative.

2. Calculate the precision by dividing the number of true positives by the sum of the number of true positives and false positives.

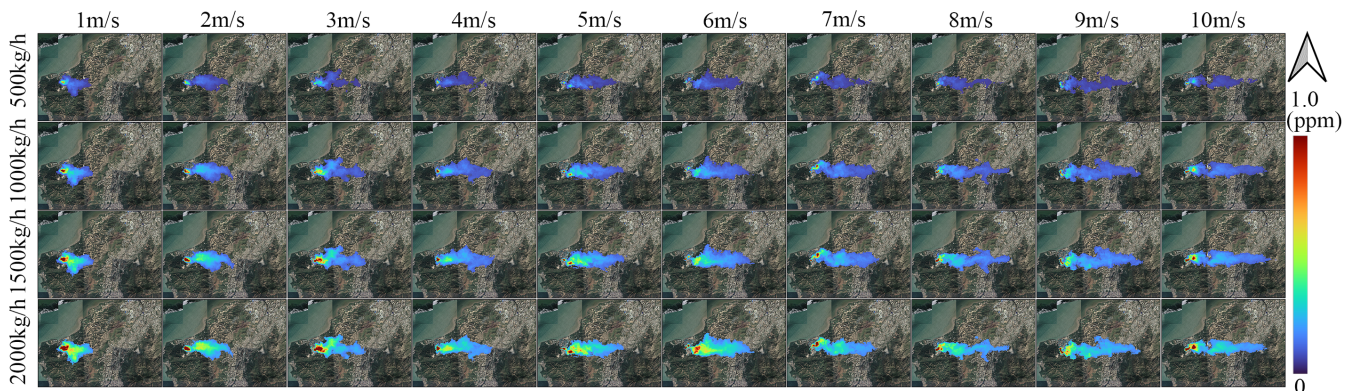


Fig. 4: Simulated methane plumes

$$Precision = \frac{TP}{TP + FP} \quad (22)$$

3. Calculate the recall by dividing the number of true positives by the sum of the number of true positives and false negatives.

$$Recall = \frac{TP}{TP + FN} \quad (23)$$

4. Repeat this process for different thresholds to obtain a set of precision and recall values.

5. Calculate the AP value:

$$AP = \sum_{i=1}^{n-1} (R_{i+1} - R_i) P_{inter}(R_i + 1) \quad (24)$$

where $(R_{i+1} - R_i)$ is the length of recall interval, and $P_{inter}(R_i + 1)$ is the interpolated precision at recall $R_i + 1$. The AP value is calculated by summing up all the interpolated precision values weighted by the lengths of recall intervals between adjacent recalls.

IV. RESULTS AND DISCUSSIONS

A. Simulation

To validate the accuracy of the simulated plumes, we refer to relevant literature[14]. The integrated methane emission (IME) values of a reasonable methane plume should be positively correlated to its emission rate. Fitting the line curve of the IME values of all simulated plumes and corresponding emission rates, the coefficient of determination reaches 0.861(Fig. 6). Therefore, we can conclude that the quality of simulated methane plumes are reasonable to large extent.

We employed an end-to-end approach to validate simulated PRISMA images. First, the methane signals in original PRISMA images were removed to generate the base map. Then, simulated methane signals were added to the base maps to obtain simulated PRISMA satellite images. Finally, methane plumes from simulated PRISMA images are detected again using Mag1c. As shown in Fig. 7, the methane plume detected by Mag1c from a simulated PRISMA image is very similar to the simulated plume which was added to the base map. But the plumes decoded by Mag1c contain more noisy pixels. This implies that the simulated PRISMA images are generally of good quality.

B. Methane Concentration Inversion

All models were evaluated on the validation dataset for methane concentration inversion(Table I). We also introduced a "mask" mechanism to Mag1c, where water body pixels are excluded from the inversion. For deep learning models, considering the importance of absorption peaks in the spectrum curve for methane concentration inversion, we chose two methods to normalize the hyperspectral data (STD1): one makes use of the same mean and standard deviation to normalize all image spectral bands, while the other one involved normalization of each band separately (STD2). The results showed that regardless of the normalization method used, the U-net model achieved higher accuracy in methane concentration inversion on the validation set compared to Mag1c. The U-net model with STD1 outperformed the one with STD2 on the validation set, indicating that preserving the shape of the spectral curve is a more reasonable choice. Interestingly, the performance of Mag1c with the "mask" mechanism was worse than the original one. This may be due to the fact that during the

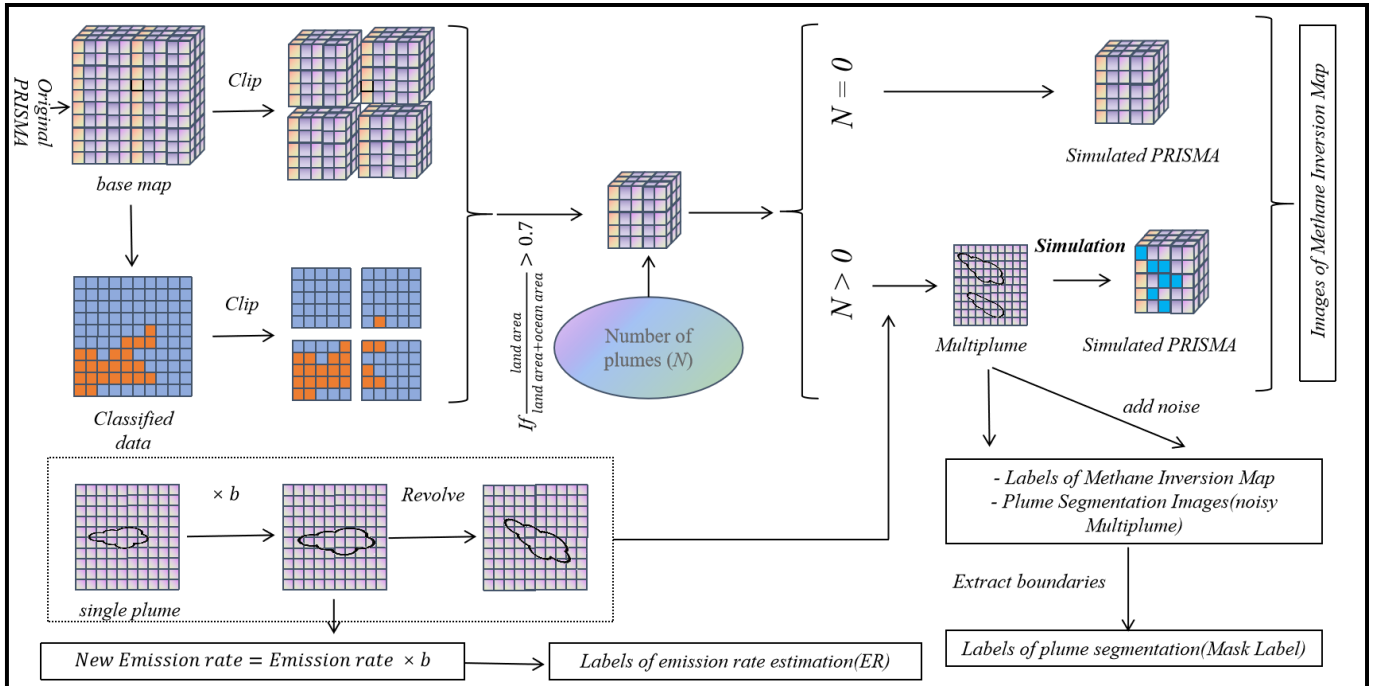


Fig. 5: Dataset simulation and generation process

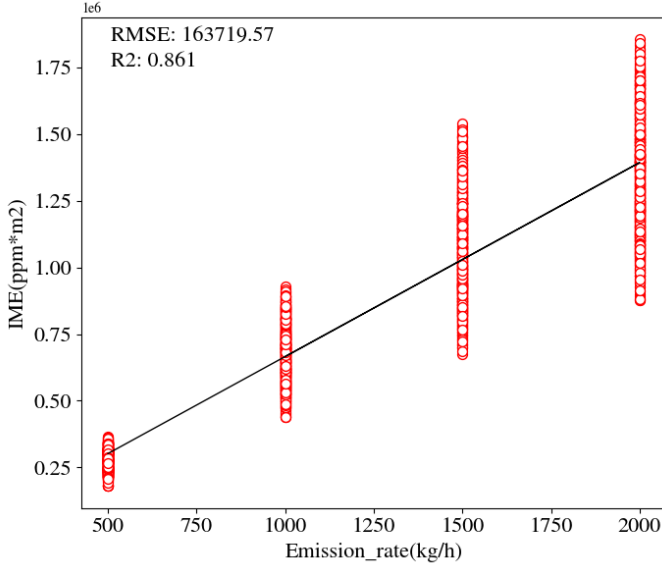


Fig. 6: Correlation between emission rates and IME values of simulated plume dataset.

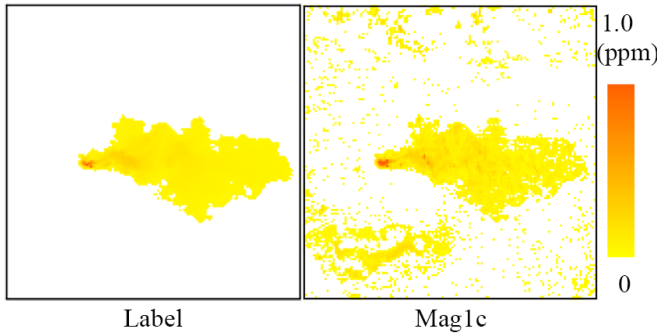


Fig. 7: The results of end-to-end verification for simulation.

“mask” process, many pixels are excluded from the inversion calculation, leading to the inability of Mag1c to fully utilize the information contained and resulting in unstable inversion results[11][42][29].

TABLE I: VALIDATION RESULTS OF METHANE CONCENTRATION INVERSION

Methods	RMSE/ppm	MAE/ppm
Mag1c	0.6371	0.0306
Mag1c + mask	1.1801	0.0850
STD1+ U-net + Smooth L_1 loss	0.0568	0.0197
STD2+ U-net + Smooth L_1 loss	0.0516	0.0142
MTL-02	0.0522	0.0104

C. Methane Plume Segmentation

We trained the Mask R-CNN model using two versions of the plume segmentation dataset described in Section A. One version used simulated hyperspectral images as inputs (hyper), while the other version used methane plume distribution maps (single). However, the labels for both versions of the dataset were identical. Similarly, we validated the models separately using validation sets corresponding to two versions of the

dataset with identical labels. Note that Active Contour method was only validated by using methane plume maps (single) as inputs, since it is an unsupervised image segmentation method which needs to explicitly relate the pixel values to task-dependent physical property. The results showed that the Mask R-CNN model achieved higher accuracy than Active Contour (Table II, Fig. 8). However, when considering the AP value at AP_{95} , Active Contour delivered higher accuracy than Mask R-CNN, which indicates that Active Contour model outperforms when extracting masks of isolated plumes. The reason why Active Contour has lower overall accuracy than Mask R-CNN could be due to that Active Contour cannot effectively separate overlapping plumes and tends to generate small noisy objects in the segmentation process. In terms of

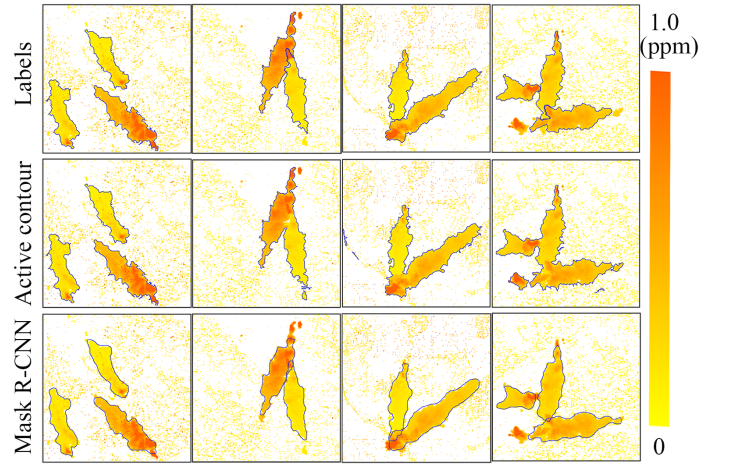


Fig. 8: Plume segmentation results of different algorithms

performance on the two versions of the dataset, Mask R-CNN had significantly higher accuracy by using the methane plume distribution map as input rather than hyperspectral images. There are two reasons for this. First, directly segmenting methane plumes from hyperspectral images involves both methane concentration inversion and plume segmentation tasks, which is more complicated. Secondly, there may exist errors in the plume signal simulation process.

TABLE II: VALIDATION RESULTS OF METHANE PLUME SEGEMENTATION

Models	AP_{50}	AP_{75}	AP_{90}	AP_{95}	$AP_{50:95}$
Active Contour	37.127	33.421	31.317	11.535	31.824
MTL-01	94.195	92.041	43.009	0.0	77.443
Mask R-CNN single	91.756	88.427	34.625	0	73.761
Mask R-CNN hyper	68.754	33.629	0	0	34.871
MTL-02	66.268	36.406	0	0	35.389

D. Estimation of Methane Emission Rate

We trained ResNet-50 and AlexNet for emission rate estimation using the training sample set, and validated the model estimation accuracy on the corresponding validation set (Table III).

The accuracy of the IME algorithm for emission rate estimation was also evaluated on the validation set. The results

showed that ResNet-50 outperformed the IME algorithm on the validation set. We have additionally validate AlexNet for the task, and the accuracy for emission rate estimation of AlexNet is slightly higher than that of the IME algorithm, but lower than that of ResNet-50. Compared to ResNet-50, a deeper network implies a better capability of nonlinear representation, allowing the learning of more complex mappings[34]. Additionally, each layer can perform its task more simply, enhancing the generalization and robustness of the network.

TABLE III: VALIDATION RESULTS OF EMISSION RATE ESTIMATION OF SINGLE NETWORKS

Methods	RMSE/ $kg * h^{-1}$	MAE/ $kg * h^{-1}$
IME	342.71	253.43
ResNet + MSE loss	172.81	133.45
AlexNet + MSE loss	329.93	245.55

E. Serial Network

Although individual models achieved high accuracy for every single tasks, the effectiveness of the serialization of multi-network models still deserves further discussion. First, we serialized Mask R-CNN and ResNet-50 to perform the task of segmenting methane plumes from concentration maps and estimating their emission rates. We evaluated the accuracy of emission rate estimation on the validation set under three conditions: 1. If segmented plumes are true positives, we estimated the emission rate using pre-trained ResNet-50 for comparison with the label's emission rate. 2. If segmented plumes are false positives, we similarly estimated its emission rate using ResNet-50 for comparison with 0 kg/h. 3. For misdetected plumes, we assumed their emission rate estimates as 0 kg/h and compared with corresponding labels. Finally, the RMSE and MAE between all predicted emission rates and label values are calculated(Table IV). We found that the accuracy of Mask R-CNN + ResNet-50 for emission rate estimation is significantly lower than that of using ResNet-50 for single-task emission rate estimation. It indicates that serializing Mask R-CNN and ResNet-50 could introduce additional errors for overall performance of methane flux rate estimation.

TABLE IV: VALIDATION RESULTS OF EMISSION RATE ESTIMATION OF SERIAL NETWORKS

Methods	RMSE/ $kg * h^{-1}$	MAE/ $kg * h^{-1}$
ResNet-50 + MSE loss	172.81	133.45
Mask R-CNN+ResNet plume	846.56	503.53
Mask R-CNN+ResNet <i>plume</i> ₃₀₀	846.06	503.44
MTL-01	714.07	433.35

To further explore the additional error sources, we selected the segmented plumes with large errors (e.g. greater than 500 kg/h). The results revealed two sources of additional errors: 1. Errors caused by small patches that actually contain only noises; 2. Errors caused by false positive patches.

We also studied the distribution of small noise patches and found that the majority are characterized by mask size of smaller than 300 pixels, whereas real plume mask size is rarely smaller than 300 pixels. Therefore, we removed segmented

masks whose size are smaller than 300 pixels and revalidated the accuracy of Mask R-CNN + ResNet-50 for emission rate estimation.

F. Multi-task Learning I (MTL-01)

We trained the *MTL-01* network and after 30 epochs of training, *MTL-01* achieved higher accuracy in the problem of plume segmentation compared to training Mask R-CNN alone. Consequently, the loss in estimating the emission rate of multiple methane flows was also smaller than in the case of serializing *Mask R-CNN* and *ResNet-50*. Furthermore, we simulated a smaller dataset to train the networks using the two approaches, and *MTL-01* exhibited even greater accuracy compared to serializing *Mask R-CNN* and *MTL-01*.

We can observe that the segmentation of additional plumes are suppressed(Fig. 9), thereby reducing the estimated emission rate. *MTL-01* tends to segment main parts of the jet stream, ignoring some smaller tail parts. This has brought improvements to both the task of plume segmentation and emission rate estimation(Table II, Table IV).

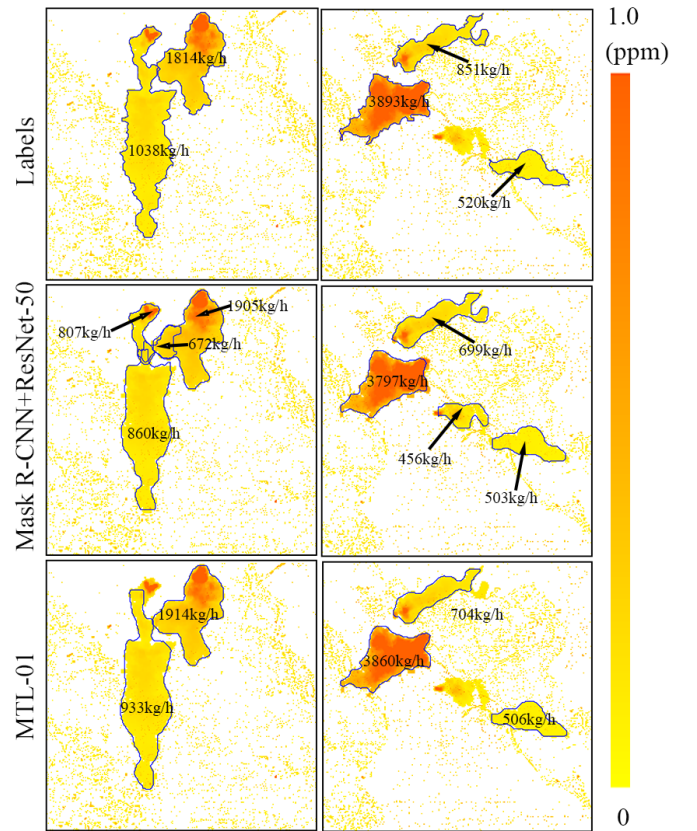


Fig. 9: Comparison of serial networks and multi-task learning I (MTL-01).

G. Multi-task Learning II (MTL-02)

We trained the MTL-02 model, which converged after 30 epochs, with both the loss function values and validation accuracy values rapidly decreasing. Ultimately, MTL-02 achieved

slightly higher accuracy in methane concentration inversion compared to U-net(Table I), and higher accuracy in plume segmentation compared to Hyper Mask R-CNN(Table II). This confirms the viewpoint that multi-task learning could improve the convergence speed and fitting accuracy of the model. This may be attributed to the shared information among multiple types of labels.

H. Limitations

Methane plume monitoring is a highly complex problem, and the current research in this field is not yet deeply explored and systematic. Our proposed approach also has some limitations: 1. The shape of plumes we simulated almost complies with standard Gaussian model, which actually is an ideal condition. But in reality, methane point source emissions are characterized by various factors such as topography and humidity, resulting in non-Gaussian plumes. Whether our approach is applicable to non-Gaussian plumes still needs further discussion; 2. The maximum overlap ratio of the plumes we studied is 15%. However, in nature, there are many methane emission sources located close to each other, and the overlap ratio of two plumes could be much higher than 15%. In such cases, despite that we can successfully generate highly overlapped methane plumes, it is difficult to provide accurate training labels and requires exploring point-based semi-supervised learning methods to achieve reasonable segmentation results for such highly overlapped plumes; 3. The acquisition of hyperspectral satellite images is greatly affected by weather conditions, and in low-latitude coastal areas, hyperspectral image data sources are sparse. Therefore, a solution that only utilizes hyperspectral images as data source may not meet high-frequency monitoring requirement. It is necessary to develop an ensemble estimation approach based on multiple data sources.

V. CONCLUSION

Currently, there are high uncertainties in fugitive methane emission monitoring methods using satellite imaging spectrometer. We have developed a demonstrative approach that utilizes deep learning models and simulated hyperspectral images for methane concentration inversion, plume segmentation, and emission rate estimation in landfills. Specifically, we employed U-net for methane concentration inversion, achieving higher accuracy and reduced noise compared to mag1c. We utilized Mask R-CNN for plume segmentation, avoiding subjectivity in the segmentation process. For methane plume emission rate estimation, ResNet-50 is employed to overcome the reliance on wind speed observations. We also discussed the additional errors of emission rate estimation introduced by serial networks and addressed this issue by training a multi-task model (MTL-01) to suppress the errors and improve the precision of plume segmentation. Additionally, a multi-task model (MTL-02) that simultaneously performs methane concentration inversion and plume segmentation is proposed, achieving higher validation accuracy than individual single-task models. Finally, we also indicated the limitations of the current approach, highlighting the need for future research

into highly overlapped plumps, non-Gaussian plumes, and the synthesis of multi-source data for inversion.

ACKNOWLEDGMENT

The work described in this paper was substantially supported by a grant from the ECF and EPD of the Hong Kong Special Administrative Region, China (Project No. PolyU ECF111/2020).

REFERENCES

- [1] Giancarlo Alfonsi. “Reynolds-Averaged Navier–Stokes Equations for Turbulence Modeling”. In: *Applied Mechanics Reviews* 62.4 (June 2009), p. 040802.
- [2] J Bogner et al. “Waste management in climate change 2007: Mitigation. contribution of working group iii to the fourth assessment report of the intergovernmental panel on climate change”. In: *Cambridge University Press, Cambridge* (2007).
- [3] David Brüggemann et al. “Exploring relational context for multi-task dense prediction”. In: *Proceedings of the IEEE/CVF international conference on computer vision*. 2021, pp. 15869–15878.
- [4] Josep G Canadell et al. *Global carbon and other biogeochemical cycles and feedbacks*. 2021.
- [5] Liang-Chieh Chen et al. “Deeplab: Semantic image segmentation with deep convolutional nets, atrous convolution, and fully connected crfs”. In: *IEEE transactions on pattern analysis and machine intelligence* 40.4 (2017), pp. 834–848.
- [6] Sergio Cogliati et al. “The PRISMA imaging spectroscopy mission: Overview and first performance analysis”. In: *Remote Sensing of Environment* 262 (2021), p. 112499.
- [7] Philip E Dennison et al. “High spatial resolution mapping of elevated atmospheric carbon dioxide using airborne imaging spectroscopy: Radiative transfer modeling and power plant plume detection”. In: *Remote Sensing of Environment* 139 (2013), pp. 116–129.
- [8] J Andrzej Domaradzki and Eileen M Saiki. “A subgrid-scale model based on the estimation of unresolved scales of turbulence”. In: *Physics of Fluids* 9.7 (1997), pp. 2148–2164.
- [9] Markus D Foote et al. “Fast and accurate retrieval of methane concentration from imaging spectrometer data using sparsity prior”. In: *IEEE Transactions on Geoscience and Remote Sensing* 58.9 (2020), pp. 6480–6492.
- [10] Markus D Foote et al. “Impact of scene-specific enhancement spectra on matched filter greenhouse gas retrievals from imaging spectroscopy”. In: *Remote Sensing of Environment* 264 (2021), p. 112574.
- [11] Christopher C Funk et al. “Clustering to improve matched filter detection of weak gas plumes in hyperspectral thermal imagery”. In: *IEEE transactions on geoscience and remote sensing* 39.7 (2001), pp. 1410–1420.

- [12] Massimo Germano et al. “A dynamic subgrid-scale eddy viscosity model”. In: *Physics of Fluids A: Fluid Dynamics* 3.7 (1991), pp. 1760–1765.
- [13] Joseph Yossi Gil and Ron Kimmel. “Efficient dilation, erosion, opening, and closing algorithms”. In: *IEEE Transactions on Pattern Analysis and Machine Intelligence* 24.12 (2002), pp. 1606–1617.
- [14] Javier Gorroño et al. “Understanding the potential of Sentinel-2 for monitoring methane point emissions”. In: *Atmospheric Measurement Techniques* 16.1 (2023), pp. 89–107.
- [15] Luis Guanter et al. “Mapping methane point emissions with the PRISMA spaceborne imaging spectrometer”. In: *Remote Sensing of Environment* 265 (2021), p. 112671.
- [16] Kaiming He et al. “Deep residual learning for image recognition”. In: *Proceedings of the IEEE conference on computer vision and pattern recognition*. 2016, pp. 770–778.
- [17] Kaiming He et al. “Mask r-cnn”. In: *Proceedings of the IEEE international conference on computer vision*. 2017, pp. 2961–2969.
- [18] Kaiming He et al. “Spatial pyramid pooling in deep convolutional networks for visual recognition”. In: *IEEE transactions on pattern analysis and machine intelligence* 37.9 (2015), pp. 1904–1916.
- [19] Kun He et al. “Hashing as tie-aware learning to rank”. In: *Proceedings of the IEEE Conference on Computer Vision and Pattern Recognition*. 2018, pp. 4023–4032.
- [20] A Iravanian and Sh O Ravari. “Types of contamination in landfills and effects on the environment: a review study”. In: *IOP Conference Series: Earth and Environmental Science*. Vol. 614. 1. IOP Publishing. 2020, p. 012083.
- [21] Shaocheng Jia and Wei Yao. “Joint learning of frequency and spatial domains for dense image prediction”. In: *ISPRS Journal of Photogrammetry and Remote Sensing* 195 (2023), pp. 14–28. ISSN: 0924-2716.
- [22] Shenlu Jiang et al. “Space-to-speed architecture supporting acceleration on VHR image processing”. In: *ISPRS Journal of Photogrammetry and Remote Sensing* 198 (2023), pp. 30–44. ISSN: 0924-2716.
- [23] Siraput Jongaramrungruang et al. “MethaNet – An AI-driven approach to quantifying methane point-source emission from high-resolution 2-D plume imagery”. In: *Remote Sensing of Environment* 269 (2022), p. 112809. ISSN: 0034-4257.
- [24] Alex Krizhevsky, Ilya Sutskever, and Geoffrey E Hinton. “Imagenet classification with deep convolutional neural networks”. In: *Communications of the ACM* 60.6 (2017), pp. 84–90.
- [25] Min Lin, Qiang Chen, and Shuicheng Yan. “Network In Network”. In: *arXiv e-prints* (2013), arXiv–1312.
- [26] Shikun Liu, Edward Johns, and Andrew J Davison. “End-to-end multi-task learning with attention”. In: *Proceedings of the IEEE/CVF conference on computer vision and pattern recognition*. 2019, pp. 1871–1880.
- [27] Jonathan Long, Evan Shelhamer, and Trevor Darrell. “Fully convolutional networks for semantic segmentation”. In: *Proceedings of the IEEE conference on computer vision and pattern recognition*. 2015, pp. 3431–3440.
- [28] Cosimo Magazzino, Marco Mele, and Nicolas Schneider. “The relationship between municipal solid waste and greenhouse gas emissions: Evidence from Switzerland”. In: *Waste Management* 113 (2020), pp. 508–520.
- [29] Chunlan Mao et al. “Process performance and methane production optimizing of anaerobic co-digestion of swine manure and corn straw”. In: *Scientific Reports* 7.1 (2017), p. 9379.
- [30] Björn Maronga et al. “The Parallelized Large-Eddy Simulation Model (PALM) version 4.0 for atmospheric and oceanic flows: model formulation, recent developments, and future perspectives”. In: *Geoscientific Model Development* 8.8 (2015), pp. 2515–2551.
- [31] Przemyslaw Polewski et al. “Instance segmentation of fallen trees in aerial color infrared imagery using active multi-contour evolution with fully convolutional network-based intensity priors”. In: *ISPRS Journal of Photogrammetry and Remote Sensing* 178 (2021), pp. 297–313.
- [32] Stephen B Pope. “Turbulent flows”. In: *Measurement Science and Technology* 12.11 (2001), pp. 2020–2021.
- [33] Siegfried Raasch and Michael Sch. “PALM-A large-eddy simulation model performing on massively parallel computers”. In: *Meteorologische Zeitschrift* 10.5 (2001), pp. 363–372.
- [34] Maithra Raghu. “On the expressive power of deep neural networks”. In: (2016).
- [35] Olaf Ronneberger, Philipp Fischer, and Thomas Brox. “U-net: Convolutional networks for biomedical image segmentation”. In: *Medical Image Computing and Computer-Assisted Intervention—MICCAI 2015: 18th International Conference, Munich, Germany, October 5-9, 2015, Proceedings, Part III* 18. Springer. 2015, pp. 234–241.
- [36] Pierre Sagaut and Yu-Tai Lee. “Large eddy simulation for incompressible flows: An introduction. scientific computation series”. In: *Appl. Mech. Rev.* 55.6 (2002), B115–B116.
- [37] Muhammad Shafiq and Zhaoquan Gu. “Deep residual learning for image recognition: a survey”. In: *Applied Sciences* 12.18 (2022), p. 8972.
- [38] Jacquelyn Shelton, Przemyslaw Polewski, and Wei Yao. “U-Net for Learning and Inference of Dense Representation of Multiple Air Pollutants from Satellite Imagery”. In: *Proceedings of the 10th International Conference on Climate Informatics*. CI2020. virtual, United Kingdom: Association for Computing Machinery, 2021, pp. 128–133. ISBN: 9781450388481.
- [39] Thomas F Stocker et al. “Technical summary”. In: *Climate change 2013: the physical science basis. Contribution of Working Group I to the Fifth Assessment Report of the Intergovernmental Panel on Climate Change*. Cambridge University Press, 2013, pp. 33–115.

- [40] Juan Terven and Diana Cordova-Esparza. “A comprehensive review of YOLO: From YOLOv1 to YOLOv8 and beyond”. In: *arXiv preprint arXiv:2304.00501* (2023).
- [41] Juan Terven et al. “Loss Functions and Metrics in Deep Learning. A Review”. In: *arXiv preprint arXiv:2307.02694* (2023).
- [42] James Theiler and Bernard R Foy. “Effect of signal contamination in matched-filter detection of the signal on a cluttered background”. In: *IEEE Geoscience and Remote Sensing Letters* 3.1 (2006), pp. 98–102.
- [43] David R Thompson et al. “Atmospheric correction for global mapping spectroscopy: ATREM advances for the HypIRI preparatory campaign”. In: *Remote Sensing of Environment* 167 (2015), pp. 64–77.
- [44] Andrew K Thorpe et al. “Airborne DOAS retrievals of methane, carbon dioxide, and water vapor concentrations at high spatial resolution: application to AVIRIS-NG”. In: *Atmospheric Measurement Techniques* 10.10 (2017), pp. 3833–3850.
- [45] Andrew K Thorpe et al. “High resolution mapping of methane emissions from marine and terrestrial sources using a Cluster-Tuned Matched Filter technique and imaging spectrometry”. In: *Remote Sensing of Environment* 134 (2013), pp. 305–318.
- [46] Simon Vandenhende et al. “Multi-Task Learning for Dense Prediction Tasks: A Survey”. In: (2020).
- [47] Daniel J Varon et al. “Quantifying methane point sources from fine-scale satellite observations of atmospheric methane plumes”. In: *Atmospheric Measurement Techniques* 11.10 (2018), pp. 5673–5686.
- [48] Andreas Veit, Michael J Wilber, and Serge Belongie. “Residual networks behave like ensembles of relatively shallow networks”. In: *Advances in neural information processing systems* 29 (2016).
- [49] Xinlong Wang et al. “Solov2: Dynamic and fast instance segmentation”. In: *Advances in Neural information processing systems* 33 (2020), pp. 17721–17732.
- [50] Zhiming Yang, Shigemi Kagawa, and Jing Li. “Do greenhouse gas emissions drive extreme weather conditions at the city level in China? Evidence from spatial effects analysis”. In: *Urban Climate* 37 (2021), p. 100812.
- [51] Ning Zang et al. “Land-use mapping for high-spatial resolution remote sensing image via deep learning: A review”. In: *IEEE Journal of Selected Topics in Applied Earth Observations and Remote Sensing* 14 (2021), pp. 5372–5391.
- [52] Chengliang Zhang et al. “Greenhouse gas emissions from landfills: A review and bibliometric analysis”. In: *Sustainability* 11.8 (2019), p. 2282.
- [53] Lichen Zhou, Chuang Zhang, and Ming Wu. “D-LinkNet: LinkNet with pretrained encoder and dilated convolution for high resolution satellite imagery road extraction”. In: *Proceedings of the IEEE conference on computer vision and pattern recognition workshops*. 2018, pp. 182–186.